Title

Multiple Regimes and Low-Frequency Variability in the Quasi-Adiabatic Overturning Circulation

Journal

Journal of Physical Oceanography, 45(6)

ISSN

0022-3670

Authors

Wolfe, Christopher L
Cessi, Paola

Publication Date

2015-06-01

DOI

10.1175/jpo-d-14-0095.1

Peer reviewed

Multiple Regimes and Low-Frequency Variability in the Quasi-Adiabatic Overturning Circulation

CHRISTOPHER L. WOLFE

School of Marine and Atmospheric Sciences, Stony Brook University, Stony Brook, New York

PAOLA CESSI

Scripps Institution of Oceanography, University of California, San Diego, La Jolla, California

(Manuscript received 12 May 2014, in final form 4 March 2015)

ABSTRACT

When interior mixing is weak, the ocean can support an interhemispheric overturning circulation on isopycnals that outcrop in both the Northern Hemisphere and a high-latitude southern circumpolar channel. This overturning cell participates in a salt–advection feedback that counteracts the precipitation-induced surface freshening of the northern high latitudes. The net result is an increase in the range of isopycnals shared between the two hemispheres, which strengthens the overturning circulation. However, if precipitation in the Northern Hemisphere sufficiently exceeds that in the Southern Hemisphere, the overturning cell collapses and is replaced by a cell circulating in the opposite direction, whose southern end point is equatorward of the channel. This reversed cell is shallower and weaker than its forward counterpart and is maintained diffusively. For a limited range of parameters, freshwater hysteresis occurs and multiple overturning regimes are found for the same forcing. These multiple regimes are, by definition, unstable with regard to finite-amplitude disturbances, since a sufficiently large perturbation can affect a transition from one regime to the other. Both overturning regimes show pronounced, nearly periodic thermohaline variability on multidecadal and multicentennial time scales. The multidecadal oscillation is expressed in the North Hemisphere gyre and driven by a surface thermohaline instability. The multicentennial oscillation has the character of an interhemispheric loop oscillation. These oscillations mediate transitions between overturning regimes by providing an internal source of finite-amplitude disturbances. As the diffusivity is reduced, the reverse cell becomes weaker and thus less stable to a given perturbation amplitude. This causes the width of the hysteresis to decrease with decreasing diffusivity.

1. Introduction

The Atlantic meridional overturning circulation (AMOC) is a planetary-scale pattern of oceanic flow responsible for about 1 PW (1 PW = 10^{15} Watts) of northward heat transport in the Atlantic Ocean (Ganachaud and Wunsch 2003; Talley 2013). Changes in the North Atlantic climate have been clearly accompanied by changes in the AMOC (McManus et al. 2004; Liu et al. 2009), with the causal relation going in both directions.

Particularly significant changes in the North Atlantic climate are possible if the AMOC is bistable, since perturbations may cause the AMOC to transition to a new stable regime (Rahmstorf 2000). The possibility of multiple stable AMOC states was first noted by Stommel (1961) and ascribed to a salt–advection feedback where the flow itself maintains the high northern salinity necessary for deep-water formation by drawing salty subtropical waters northward. The salt–advection feedback has since been shown to lead to multiple AMOC equilibria in models of increasing complexity: from zonally averaged ocean models to intermediate complexity climate models with fully three-dimensional ocean general circulation models [see Rahmstorf et al. (2005) for a review]. In models, the transition from one stable AMOC state to the other is often initiated by a freshwater perturbation added to the northern deep-water formation region (‘‘hosing’’ experiments). Freshwater hystereses are rarely observed in fully coupled

Corresponding author address: Christopher L. Wolfe, School of Marine and Atmospheric Sciences, 100 Nicolls Rd., Stony Brook University, Stony Brook, NY 11794-5000.
E-mail: christopher.wolfe@stonybrook.edu

DOI: 10.1175/JPO-D-14-0095.1

climate models (Schmitner et al. 2005; Schlesinger et al. 2006), leading Hofmann and Rahmstorf (2009) to speculate that the tuning required to make these models produce realistic climates leads to excessively stable AMOCs.

The overturning circulation in Stommel's (1961) box model is necessarily diffusively driven, since each box is assumed to be completely and instantaneously mixed. The majority of hosing experiments since Stommel (1961) have also operated in a diffusive regime, either through large explicit diapycnal diffusivities, advection schemes with large implicit numerical diffusivities, or substantial implicit diapycnal diffusion due to large horizontal, rather than isopycnal, mixing (Hofmann and Morales Maqueda 2006; Hofmann and Rahmstorf 2009). In the diffusive regime, the AMOC is driven by the density difference between the subpolar North Atlantic and the upwelling end point (either the subtropics or the Southern Ocean); in this context, the advection of salt by the circulation reinforces the density difference set by the temperature distribution (Stommel 1961; Rooth 1982; Bryan 1986; Cessi and Young 1992; Rahmstorf 1996).

Observations (Ledwell et al. 1993; Kunze and Sanford 1996; Gregg et al. 2003; Kunze et al. 2006; Waterman et al. 2014) suggest that the mixing rate in the World Ocean is sufficiently low that the AMOC is quasi-adiabatic, with flow in the Atlantic basin largely along isopycnals. In this context, the Southern Ocean (SO) wind-driven upwelling plays a significant role in powering the circulation (Toggweiler and Samuels 1995; Marshall and Speer 2012; Talley 2013). For a given SO wind stress, the strength of the quasi-adiabatic AMOC is controlled by the range of surface buoyancy common to the Antarctic Circumpolar Current (ACC) and the Northern Hemisphere (NH) (Wolfe and Cessi 2010, 2011; Nikurashin and Vallis 2012). Wolfe and Cessi (2014) have shown that, in the quasi-adiabatic regime, the salt–advection feedback increases the range of surface buoyancies shared between the ACC and the NH (i.e., decreases the pole-to-pole buoyancy difference), strengthening the AMOC. This effect is the opposite of the traditional salt feedback mechanism in the diffusive regime, which increases the buoyancy difference between the hemispheres.

The dominant role of the Southern Ocean in the AMOC has led some authors to argue that the quasi-adiabatic AMOC is monostable (e.g., Gnanadesikan and Toggweiler 1999; Keeling 2002; Nof et al. 2007); however, several theoretical (Johnson et al. 2007; Fürst and Levermann 2012; Cimatoribus et al. 2014) studies and experiments with coupled climate models (Hofmann and Rahmstorf 2009) have shown that the quasi-adiabatic MOC does, in fact, possess multiple stable states.

This paper reports a series of hosing experiments using a general circulation model in a simplified domain, representing the Atlantic sector of the World Ocean and subject to idealized forcing. We consider smaller diffusivities than Hofmann and Rahmstorf (2009) and the absence of a Pacific Ocean results in a circulation that is necessarily less diffusive than could be obtained in a global model. The existence of multiple regimes is found to be robust in the quasi-adiabatic AMOC and is attributed to the action of the salt–advection feedback.

The multiple regimes found in our experiments are not, in general, equilibria, but show pronounced, nearly periodic variability on superannual, multidecadal, and multicentennial time scales. Such intrinsic thermohaline variability arises spontaneously in idealized ocean circulation models if dissipation is sufficiently weak (Huang and Chou 1994; Greatbatch and Zhang 1995; Huck et al. 1999, 2015). The superannual variability is because of an instability of the equatorial current systems and does not appear to significantly affect the MOC. In contrast, the multidecadal and multicentennial oscillations are basin-scale modulations in the strength of the MOC that increase in amplitude near the transitions between MOC regimes. While low-frequency (particularly multidecadal) thermohaline variability has been a subject of intense study over the past few decades [see, e.g., Dijkstra and Ghil (2005), Grossmann and Klotzbach (2009), and Liu (2012) for reviews], the relationship between this variability and thermohaline hysteresis has received less attention. In addition, internally driven, low-frequency oscillations have been mostly analyzed in the context of one hemisphere diffusive overturning circulations (e.g., Colin de Verdière and Huck 1999; te Raa and Dijkstra 2002; Arzel et al. 2006; Sévellec et al. 2010; Dijkstra et al. 2014). Sévellec et al. (2006) considered an interhemispherical geometry driven by surface thermal and haline forcing only (no wind) but found that centennial oscillations are not sustained in this configuration.

Our approach to this question is to examine the role of buoyancy forcing, and in particular of the freshwater flux, in the interhemispheric overturning circulation through a series of idealized process studies using an oceanic general circulation model. The model and diagnostics are described in section 2. The emergence of multiple regimes and hysteresis is discussed in section 3. The intrinsic time dependence is discussed in section 4, and concluding remarks are given in section 5.

2. Model and diagnostics

The model used herein is described in detail in Wolfe and Cessi (2014); a brief summary of the configuration is given here for completeness.

We use the Massachusetts Institute of Technology general circulation model (MITgcm; Marshall et al. 1997a,b) to integrate the hydrostatic, Boussinesq primitive equations in a rectangular, equatorially centered β plane with zonal and meridional extents of $L_x = 2500$ km and $2L_y = 10\,000$ km, respectively, and a depth of $H = 2400$ m. The model has a flat bottom and vertical walls, except for the range $-L_y \le y \le -3750$ km, which is a zonally reentrant channel. The horizontal resolution is 100 km. There are 20 levels in the vertical with thicknesses ranging from 12 m near the surface to 225 m near the bottom.

Tracers are advected using the second-order moments (SOM) scheme of Prather (1986) and diffused using a vertical diffusivity that is surface intensified to model an idealized mixed layer of depth $d = 40$ m. The vertical diffusivity has the form

$$\kappa_v(z) = \kappa_a + \frac{1}{2}\kappa_s\left[1 + \tanh\left(\frac{z+d}{\delta_{\rm mix}}\right)\right], \qquad (1)$$

where $\delta_{\rm mix} = 3$ m, and the surface diffusivity $\kappa_s = 5 \times 10^{-3}\,{\rm m^2\,s^{-1}}$. Two values for the abyssal diffusivity κ_a are considered, both well below the canonical Munk (1966) value of $10^{-4}\,{\rm m^2\,s^{-1}}$: a moderate-diffusivity (MOD-DIFF) case with $\kappa_a = 2.5 \times 10^{-5}\,{\rm m^2\,s^{-1}}$ and a low-diffusivity (LOW-DIFF) case with $\kappa_a = 3.125 \times 10^{-6}\,{\rm m^2\,s^{-1}}$. The lowest value of κ_a is near, but above, the value at which numerical diffusion due to the SOM scheme overwhelms explicit diffusion. An analysis similar to Griffies et al. (2000) finds that the effective abyssal diffusivity due to the combination of explicit and numerical diffusion is $2.9 \times 10^{-5}\,{\rm m^2\,s^{-1}}$ in the MOD-DIFF case and $5.1 \times 10^{-6}\,{\rm m^2\,s^{-1}}$ (6 times smaller) in the LOW-DIFF case. Thus, the contribution of numerical diffusion to mixing in these models is small and is not expected to alter the results in any meaningful way.

A linear equation of state is used with buoyancy given by

$$b = g\alpha_\theta(\theta - \theta_{\rm ref}) - g\beta_S(S - S_{\rm ref}), \qquad (2)$$

where θ is potential temperature, $\theta_{\rm ref} = 0.5$°C, S is salinity, $S_{\rm ref} = 35$ psu, g is gravitational acceleration, and the expansion coefficients are $\alpha_\theta = 2 \times 10^{-4}\,{\rm K^{-1}}$ and $\beta_S = 7.5 \times 10^{-4}\,{\rm psu^{-1}}$.

Surface-forcing functions are idealized representations of the forcing of the Atlantic Ocean. Wind stress is purely zonal and is shown in Fig. 1. The SST (i.e., the temperature in the top level) is relaxed with a time scale of 10 days to the profile

$$T^\star(y) = T^\star_{\rm eq}\cos^2\frac{\pi y}{2L_y} + T^\star_{\rm N}\exp[-(y - L_y)^2/\delta_T^2], \qquad (3)$$

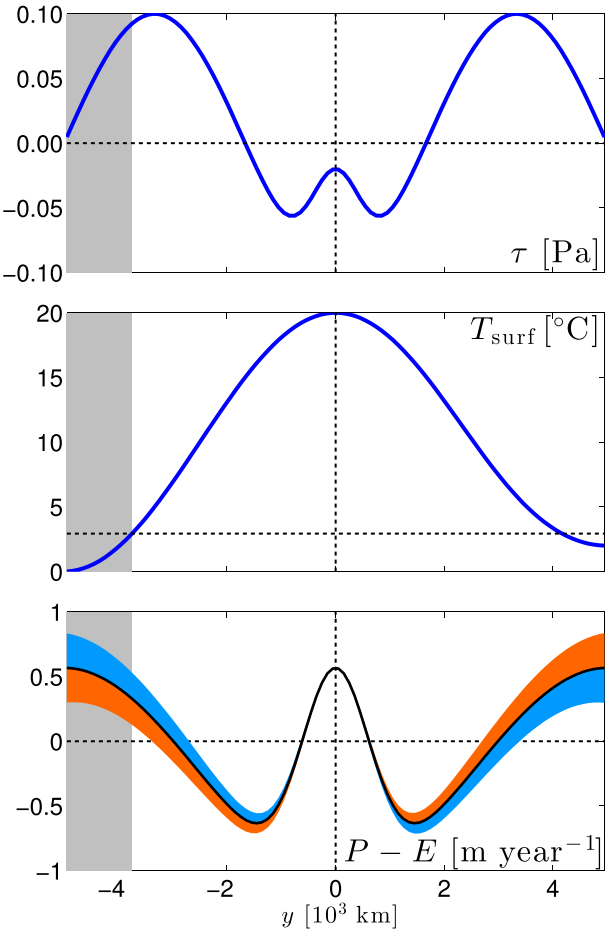

FIG. 1. (top) Zonal wind stress τ, (middle) SST relaxation profile T^* given in (3), and (bottom) precipitation minus evaporation $P - E$ given in (4) as a function of meridional position y. The gray shaded region gives the latitude band of the channel. In the middle panel, the horizontal dashed line denotes the temperature at the northern edge of the channel. The bottom panel gives the range of possible freshwater flux profiles used in Fig. 4, obtained by varying ΔF.

where $T^\star_{\rm eq} = 20$°C, $\delta_T = 1800$ km, and the northern temperature $T^\star_{\rm N} = 2$°C. The short relaxation time scale ensures that the mixed layer temperature is nearly clamped to the relaxation profile. Surface freshwater forcing is represented by a virtual salt flux[1] applied in the top level

$$\mathcal{F}(y) = -S_{\rm ref}[P - E - (P - E)_{\rm ave}], \qquad (4)$$

where the precipitation P minus evaporation E is given by

[1] Positive salt fluxes increase surface salinity.

$$P - E = -F_0 \left[\cos\frac{\pi y}{L_y} - a_S \exp(-y^2/\delta_S^2) \right] - 2\frac{\Delta F}{L_x L_y}\frac{y}{L_y}, \tag{5}$$

where $a_S = 2$, $\delta_S = 900\,\text{km}$, and $(P - E)_{\text{ave}}$ is the area average of $P - E$. We use $F_0 = 0.81\,\text{m yr}^{-1}$ and vary ΔF from -0.05 to 0.01 Sverdrups (Sv; $1\,\text{Sv} \equiv 10^6\,\text{m}^3\,\text{s}^{-1}$) to break the hemispherical symmetry of the freshwater flux. The surface-forcing functions are shown in Fig. 1.

The combination of relaxation thermal and fixed-flux freshwater boundary conditions leads to "mixed" boundary conditions on buoyancy. The use of mixed boundary conditions dates back at least to Haney (1971) and reflects the idea that surface heat fluxes tend to remove temperature differences between the atmosphere and ocean while no such feedback exists for salinity. Some authors have argued that fixed-flux thermal boundary conditions are more appropriate on decadal or longer time scales, since the atmosphere's heat capacity is so small that surface thermal anomalies should remain unaffected by atmospheric processes (e.g., Zhang et al. 1993). On the other hand, Buckley et al. (2012) found using a coupled atmosphere–ocean circulation model that decadal thermal anomalies are, in fact, damped by air–sea interactions. The specification of surface boundary conditions for long-time-scale ocean simulations thus appears to be an unresolved issue; we make use of mixed boundary conditions for their conceptual simplicity and for continuity with previous studies.

Momentum is dissipated via Laplacian viscosity with horizontal and vertical coefficients $A_h = 10^4\,\text{m}^2\,\text{s}^{-1}$ and $A_v = 2.5 \times 10^{-4}\,\text{m}^2\,\text{s}^{-1}$, respectively; we employ no-slip sidewalls and a free-slip bottom augmented by a linear bottom drag with coefficient $r = 5 \times 10^{-6}\,\text{s}^{-1}$. Because of the coarse model resolution, baroclinic eddies are parameterized using the advective form of Gent and McWilliams (1990, hereinafter GM) and Redi (1982) isopycnal mixing with equal mixing coefficients $K_{\text{GM}} = 500\,\text{m}^2\,\text{s}^{-1}$; this value was determined by matching the slopes in the model's channel with those from an eddy-resolving simulation in the same domain (Wolfe and Cessi 2011). GM is implemented using the boundary value problem scheme of Ferrari et al. (2010) with vertical mode number $m = 2$ and minimum wave speed $c_{\text{min}} = 0.1\,\text{m s}^{-1}$. The Redi tensor is tapered exponentially to horizontal diffusion in regions of weak stratification using the method of Danabasoglu and McWilliams (1995).

All simulations were run to statistical equilibrium—at least 5000 yr—and analyses performed on the final 1000 yr, except for the multicentennial oscillations for which the analysis was extended to 20 000 yr.

a. Residual overturning streamfunction

The overturning circulation is quantified using the zonally integrated residual overturning streamfunction

$$\psi(y, \tilde{b}, t) \equiv \int_0^{L_x}\int_{-H}^{0} v^\dagger(x, y, z, t)\mathcal{H}[b(x, y, z, t) - \tilde{b}]\,dz\,dx, \tag{6}$$

where $v^\dagger = v + v_{\text{GM}}$ is the total meridional velocity (the sum of the resolved velocity v and the eddy velocity from the GM parameterization v_{GM}), and $\mathcal{H}$ is the Heaviside step function. The residual streamfunction ψ is the zonally integrated transport of water above the isopycnal $b(x, y, z, t) = \tilde{b}$. The "vertical" coordinate $\tilde{b}$ is buoyancy; the tilde distinguishes the coordinate "buoyancy" from the buoyancy field.

For presentation purposes, ψ is remapped into height coordinates using the zonal-mean isopycnal height

$$\zeta(y, \tilde{b}, t) \equiv -\frac{1}{L_x}\int_0^{L_x}\int_{-H}^{0} \mathcal{H}[b(x, y, z, t) - \tilde{b}]\,dz\,dx. \tag{7}$$

In height coordinates, the time-mean residual streamfunction $\overline{\psi}$ advects a modified buoyancy $b^\#(y, z)$ that satisfies $\overline{\zeta}[y, b^\#(y, z)] = z$, where the bar denotes the time mean

$$\overline{\cdot} \equiv \frac{1}{T}\int_0^T \cdot\,dt. \tag{8}$$

The streamfunction $\overline{\psi}$ is constant on $b^\#$ contours for purely adiabatic flow (de Szoeke and Bennett 1993; McDougall and McIntosh 2001; Young 2012).[2]

Because of zonal buoyancy gradients, the remapping distorts the vertical extent of the mixed layer. We define an isopycnal labeled by $\tilde{b}$ to be in the mixed layer if

$$\frac{1}{L_x}\int_0^{L_x} \mathcal{H}(\tilde{b} - b_0 + \delta b)\,dx \geq 0, \tag{9}$$

where b_0 is the surface buoyancy, and $\delta b = 1.6 \times 10^{-3}\,\text{m s}^{-2}$ is the threshold of Kara et al. (2000); the mixed layer region is remapped into height coordinates in the same manner as ψ.

[2] Note that de Szoeke and Bennett (1993) and McDougall and McIntosh (2001) use the tilde notation $\tilde{b}$ to denote the modified buoyancy, while in Young (2012), and the present text, $\tilde{b}$ is the buoyancy coordinate and $b^\#$ is the modified buoyancy.

b. *Thickness-weighted average temperature and salinity*

The thickness-weighted average (TWA) temperature $\hat{\theta}$ and salinity $\hat{S}$ are time and zonally averaged at constant buoyancy (de Szoeke and Bennett 1993). They are defined as

$$(\hat{\theta},\hat{S})(y,\tilde{b}) \equiv \frac{1}{L_x}\int_0^{L_x}\int_{-H}^{0} \overline{(\theta,S)\delta(b-\tilde{b})}\,dz\,dx, \qquad (10)$$

where the thickness weight $\overline{\sigma} \equiv \partial_{\tilde{b}}\zeta$, and δ is the δ function. The TWA fields $\hat{\theta}$ and $\hat{S}$ are remapped into height coordinates in the same manner as ψ.

c. *Cross-equatorial heat transport*

The integral of the residual streamfunction in buoyancy space gives the meridional buoyancy transport $F_b(y, t)$; that is,

$$F_b(y,t) \equiv \int \psi\, d\tilde{b} = \int_0^{L_x}\int_{-H}^{0} v^{\dagger} b\, dz\, dx. \qquad (11)$$

The buoyancy transport across the equator $F_b(0, t)$ is thus an integral measure of the strength of the interhemispheric component of ψ. In the present experiments, the thermal contribution to $F_b(0, t)$ is two orders of magnitude larger than the haline component, so $F_b(0, t)$ is simply proportional to the cross-equatorial heat transport, defined as

$$F_Q \equiv \int_0^{L_x}\int_{-H}^{0} c_p\rho_0 v^{\dagger}\theta|_{y=0}\, dz\, dx, \qquad (12)$$

where $c_p = 4 \times 10^3\,\mathrm{J\,kg^{-1}\,K^{-1}}$ is the heat capacity. We use F_Q as an index for the strength of the interhemispheric circulation because it reflects the transport of properties better than the maximum of ψ over the domain (which depends more sensitively than F_Q on the details of the vertical grid).

3. Hysteresis and multiple regimes

When $\Delta F = 0$, the freshwater flux is symmetric about the equator and a typical interhemispheric cell is obtained, with a substantial adiabatic component in the interior. An example is shown in Fig. 2, where $\overline{\psi}$, $\hat{\theta}$, and $\hat{S} - S_{\mathrm{ref}}$ are contoured as a function of y and ζ in Figs. 2a, 2b, and 2c, respectively. Notice that, because of the reduced size of our domain (approximately one-half the length, width, and depth of the North Atlantic), the residual streamfunction is about a factor of 4 smaller than that observed in the North Atlantic, according to the adiabatic scaling (Gnanadesikan 1999; Wolfe and Cessi 2010; Nikurashin and Vallis 2012; Wolfe and Cessi 2014)

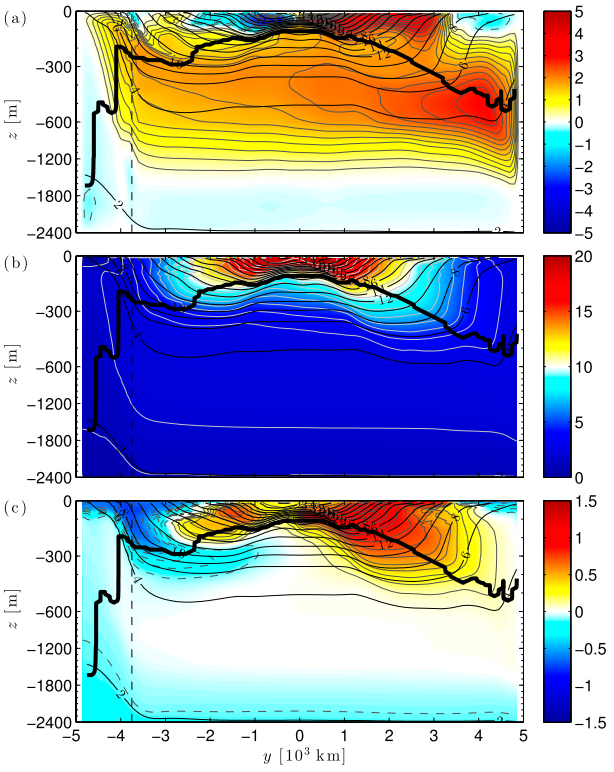

FIG. 2. (a) Mean overturning streamfunction $\overline{\psi}$ (colors/thin lines with interval 0.25 Sv) and modified buoyancy $b^{\#}$ (thick lines) for the LOW-DIFF, $\Delta F = 0$ Sv case. The thick black line gives an estimate of the base of the mixed layer. The northern edge of the channel is denoted by a vertical dashed line. (b) The TWA temperature $\hat{\theta}$ (colors/thin lines) and modified buoyancy $b^{\#}$ (thick lines). (c) The TWA salinity anomaly $\hat{S} - S_{\mathrm{ref}}$ (colors/thin lines) and modified buoyancy $b^{\#}$ (thick lines).

$$\psi \sim \Delta b h_c^2/f, \qquad (13)$$

where Δb is the range of buoyancies shared between the channel region and the Northern Hemisphere, h_c is the depth of the densest shared isopycnal at the northern edge channel, and f is the Coriolis parameter in the region of sinking. Because h_c increases approximately linearly with the meridional length of the channel, we expect the residual streamfunction to scale quadratically with the basin size.

In Fig. 2, the isopycnals $4.2 \times 10^{-3} \le b \le 11.3 \times 10^{-3}\,\mathrm{m\,s^{-2}}$ are shared between the NH and the channel. This range is more than twice as large as the range obtained from the thermal contribution alone, which is externally prescribed by the temperature relaxation condition. The widening of the range of shared surface isopycnals is due to the salt–advection feedback: the

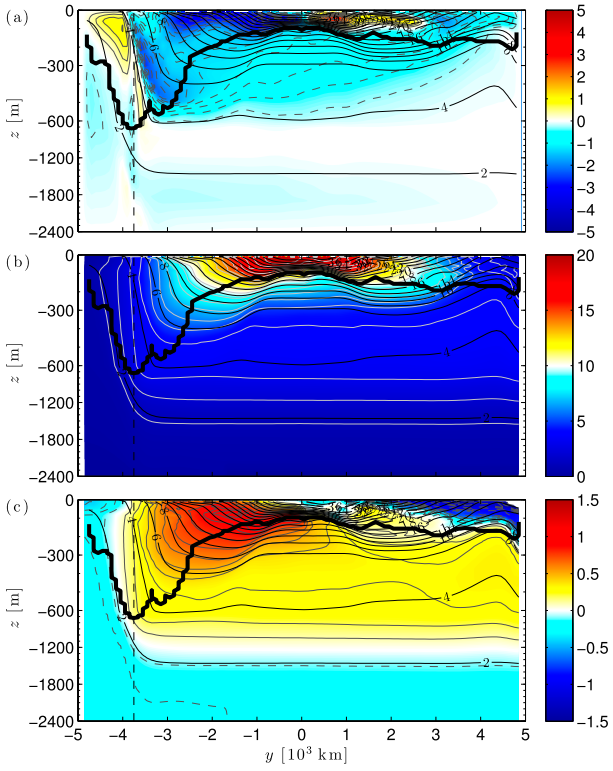

FIG. 3. As in Fig. 2, but with $\Delta F = -0.05$ Sv.

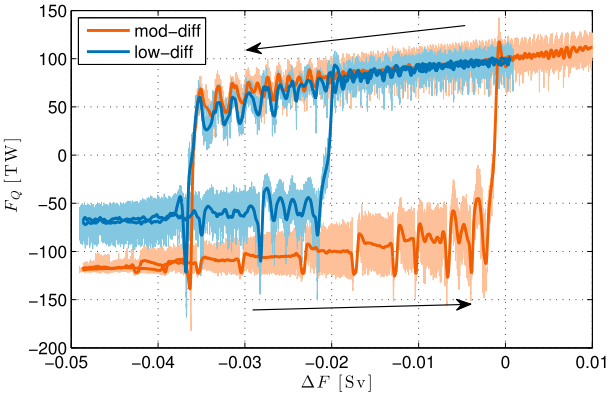

FIG. 4. The hysteresis curve in the $\Delta F - F_Q$ plane for the LOW-DIFF (blue) and MOD-DIFF (red) cases.

northward surface transport of the interhemispheric cell brings salty water of subtropical origin into the NH Subpolar Gyre, opposing the tendency due to the surface freshwater flux. Conversely, there is no surface circulation that opposes the freshening due to the prescribed surface freshwater flux in the Southern Hemisphere (SH) channel; the channel is therefore fresher than the high latitudes of the NH. This positive feedback strengthens the MOC relative to the salt-free case as discussed in Wolfe and Cessi (2014). The asymmetry in the salt distribution between the high-latitude end points of the cell increases the range of shared isopycnals Δb, which in turn increases the surface northward circulation responsible for the asymmetry, according to (13). Because of the rapid relaxation of the surface temperature to a prescribed distribution, the northward advection by the residual circulation does not induce a strong asymmetry in the temperature field (cf. Figs. 2b and 2c). For the parameter range of multiple regimes shown here, salinity and temperature contribute equally to the range of buoyancies shared between the end points of the forward cell, so temperature remains important in the determination of Δb in (13).

If ΔF is sufficiently negative, the NH surface freshening prevails over the salt–advection feedback, and surface isopycnals are no longer shared between the channel region and the NH. When this happens, the clockwise interhemispheric circulation collapses and is replaced by a weak anticlockwise (reverse) interhemispheric cell (cf. Fig. 3a). The channel region does not participate in the reverse cell because the strong upwelling in this region would oppose this circulation. Instead, this middepth cell spans the highest latitudes of the NH to the region just north of the channel but south of the SH subtropical gyre, while the channel is occupied by a Deacon cell extending to middepth. This circulation represents a short circuit of the MOC (Toggweiler and Samuels 1995; Samelson 2004; Hofmann and Rahmstorf 2009). Because the isopycnals involved in the anticlockwise interhemispheric circulation are shallower than those outcropping in the channel, the reverse cell and associated deep stratification are weaker than the forward cell (cf. Fig. 2). In the low-diffusivity regime examined here and in Hofmann and Rahmstorf (2009), the forward cell (cf. Fig. 2a) is quasi-adiabatic and powered by the wind-induced upwelling in the channel region, while the reverse cell shown in Fig. 3 is diffusive and avoids the upwelling in the channel. For the reverse cell, salt is crucial in determining the sense of circulations; salinity controls the direction of circulation (Figs. 2c), while the interhemispheric differences in the temperature field (Figs. 2b, 3b) are minimal. This is in contrast to the forward MOC, where temperature and salinity are equally important in determining the range of shared isopycnals [cf. Figs. 3b and 2c and Fig. 11 of Wolfe and Cessi (2014)].

The switch from the quasi-adiabatic forward cell to the diffusive reverse cell occurs abruptly as the salinity asymmetry parameter ΔF is changed. The abrupt transition to a qualitatively different circulation as an external parameter is changed smoothly indicates hysteresis and multiple regimes. This is illustrated in Fig. 4, where the equatorial heat transport F_Q, defined in

(12), is plotted as a function of the parameter ΔF. At two critical values of ΔF, a transition occurs in which F_Q changes sign. Although the forcing is changed linearly and quasi-adiabatically, the response is not steady but exhibits oscillations around the quasi-steady regimes. The oscillations dramatically increase in amplitude in the vicinity of the transitions. Between the two critical values of ΔF, multiple regimes are found; these solutions are quasi-steady in that they exhibit oscillations around well-defined fixed points. The solutions with positive and negative F_Q are qualitatively similar to the forward and reverse solutions found for $\Delta F = 0$ (cf. Fig. 2) and $\Delta F = 0.05$ Sv (cf. Fig. 3), respectively. The same behavior is obtained if—rather than changing the forcing quasi-adiabatically in one computation—several computations are performed, each with a different, but fixed, value of ΔF.

While hysteresis diagrams of the MOC have been shown many times before (Stommel 1961; Rooth 1982; Welander 1986; Bryan 1986; Cessi and Young 1992; Rahmstorf 1996; Dijkstra 2007; Hofmann and Rahmstorf 2009), the low-diffusivity regime examined here leads to a different character of the MOC. We demonstrate the adiabatic nature of the forward cell in Fig. 5a, which shows the range of shared surface buoyancy as a function of ΔF, with ΔF increased (forward arrow) and decreased (backward arrow). In both cases, the switch to the alternative solution is characterized by the shared surface buoyancy range $\Delta b \equiv b_C - b_N$ passing through zero, where b_N is the minimum surface buoyancy in the NH, and b_C is the maximum surface buoyancy in the channel. For the forward cell, Δb represents the range of shared buoyancies, while for the reverse cell it measures the difference in buoyancies at the cell end points. This quantity should be contrasted with the pole-to-pole buoyancy difference $b_S - b_N$, where b_S is the minimum surface buoyancy in the SH. The difference $b_S - b_N$ is the key quantity in measuring the interhemispherical gradient of buoyancy in diffusive theories (Stommel 1961; Rooth 1982; Welander 1986; Bryan 1986; Cessi and Young 1992; Rahmstorf 1996; Dijkstra 2007).

In diffusive theories, the overturning flow is assumed to be down the mean buoyancy gradient; thus, a positive overturning should have a positive value of $b_S - b_N$. However, the forward cell in our computations flows up the mean interhemispheric buoyancy difference (Fig. 5b). Furthermore, the forward cell has a smaller value of $b_S - b_N$ than the reverse cell, even though it is stronger. The reverse cell flows down the mean buoyancy gradient (measured equivalently by Δb or $b_S - b_N$), indicating that the reverse cell is diffusively driven, with an overturning strength that vanishes in the limit $\kappa_a \to 0$.

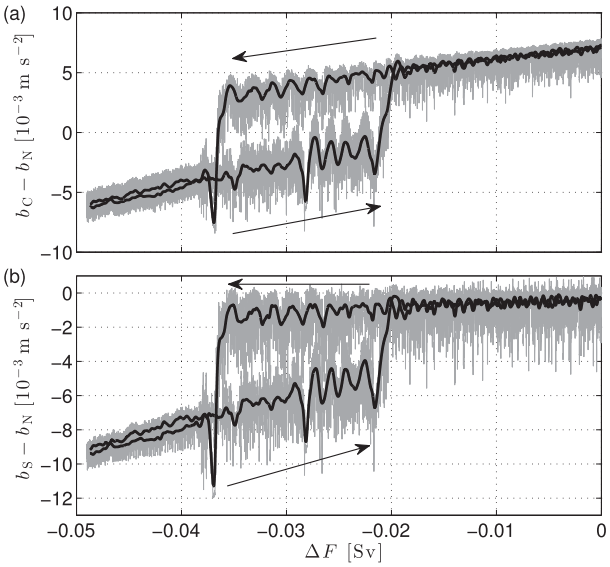

FIG. 5. (a) The range of surface buoyancy shared between the channel region and the NH, defined as the difference between the maximum buoyancy in the channel minus the minimum buoyancy in the NH, as a function of ΔF for ΔF increasing (forward arrow) and ΔF decreasing (backward arrow). (b) The interhemispheric surface buoyancy difference defined as the difference between the minimum buoyancy in the SH minus the minimum buoyancy in the NH as a function of ΔF.

In summary, the forward and reverse meridional overturning cells display qualitatively different dynamics in the quasi-adiabatic regime. The forward cell is powered by the wind stress in the channel region and flows up the interhemispheric buoyancy gradient. The reverse cell retreats north of the channel to avoid the opposing upwelling pull and flows down the interhemispheric buoyancy gradient in a diffusive balance. The existence of the forward cell relies on surface buoyancies shared between the channel region and the NH, whose range is increased by the salt–advection feedback and opposed by the imposed asymmetric temperature distribution and freshwater flux.

Figure 4 shows that the range of ΔF where multiple regimes exist increases with diffusivity. This result has been previously discussed by Prange et al. (2003) and Nof et al. (2007) and has been interpreted as proof that multiple equilibria can only exist in the diffusive regime initially envisioned by Stommel (1961). Our computations differ from those of Prange et al. (2003) and Nof et al. (2007) in that we consider a single basin and much lower diapycnal diffusivities (one order of magnitude smaller). Additionally, we parameterize mesoscale eddies—which are necessary for a proper representation of Southern Ocean upwelling—using the GM scheme. In contrast, Prange et al. (2003) and

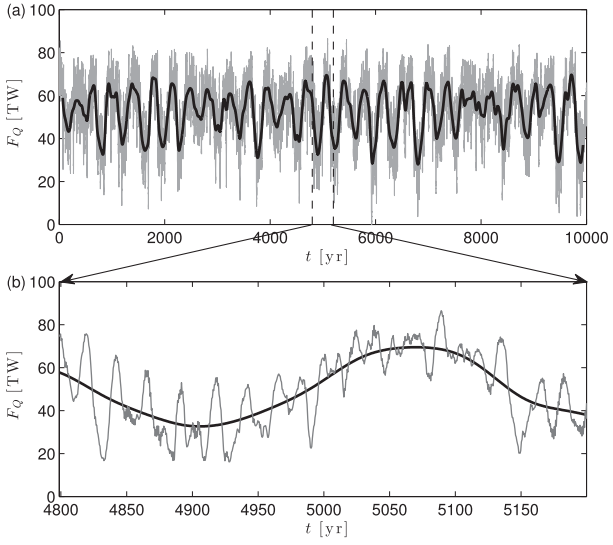

FIG. 6. (a) Time series of the cross-equatorial heat flux F_Q at half-yearly resolution (thin curves) and low-passed to retain periods of 100 yr or longer (thick curves) for a LOW-DIFF experiment with $\Delta F = -0.03$ Sv on the upper branch of Fig. 4. (b) A 400-yr segment of the same time series.

Nof et al. (2007) did not explicitly parameterize eddies. Even for our lowest value of diffusivity, both forward and reverse cells exist and have distinct amplitudes. Further reduction of the explicit diffusivity is not meaningful in z-coordinate models such as those used here because, at lower values of κ_a, diffusion due to the advection scheme destroys tracer variance at a rate comparable to the explicit diffusive terms.

The question of whether hysteresis disappears in the limit of zero diapycnal diffusivity cannot be definitively settled with a time-stepping code such as the one used here. The evidence presented here, for the lowest diffusivity achievable using one of the least diffusive advection schemes, is consistent with the notion that hysteresis persists in the adiabatic limit, as indicated by the analysis of the simple quasi-adiabatic box model of Cimatoribus et al. (2014).

4. Spontaneous time dependence

We attribute the diminishing range of hysteresis with decreased diapycnal diffusivity to the onset of spontaneous time dependence, which takes the form of finite-amplitude oscillations. For the limited region of parameter space examined, the critical value of ΔF for the onset of oscillations is independent of diffusivity for the forward, quasi-adiabatic cell but moves toward more negative values as diffusivity is increased for the reverse cell. In this way, the region of stability of the reverse cell decreases with diminishing diffusion. This dependence on diffusivity of the reverse cell's stability is not surprising, given that this mode of circulation crucially depends on the interior diapycnal processes. On the contrary, as discussed in the following, the mechanisms responsible for the oscillations around the forward cell are essentially independent of the interior diapycnal diffusivity.

TABLE 1. Period parameters (yr) used in the filter (14).

Band	τ_{low}	τ_{high}
Multidecadal	6	90
Multicentennial	120	1197
Low pass	132	∞

We now discuss the nature of the oscillations found around the forward cell, since this case is clearly in the adiabatic regime and has not been studied previously. The oscillations found at low diffusivity display three prominent time and spatial scales; Fig. 6 shows a portion of the time series for F_Q. The power spectrum of F_Q (not shown) has two broad peaks centered at 21 ± 3 and 380 ± 60 yr accounting for 36% and 42%, respectively, of the variance at subannual frequencies.[3] (The errors associated with the determination of the periods are estimated as the half-width at half maximum of the peaks.)

To isolate the two quasi-periodic signals, the time series are filtered into two frequency bands. The filtering is performed in the time domain by convolution of the time series with the bandpass taper

$$h(t;\tau_{\text{low}},\tau_{\text{high}}) = h_L(t;\tau_{\text{low}}) - h_L(t;\tau_{\text{high}}), \quad (14)$$

where

$$h_L(t;\tau) = \frac{2c_0}{t}\cos^2\frac{\pi t}{\tau}\sin\frac{2\pi t}{\tau}, \quad \text{for} \quad |t| < \frac{\tau}{2}. \quad (15)$$

The normalization constant $c_0 = 2\text{Si}(\pi) + \text{Si}(2\pi)$, where $\text{Si}(z)$ is the sine integral, ensures that the integral of h_L is unity. The coefficients for each band are given in Table 1. The spatial patterns associated with the oscillations in each band are isolated by performing a bivariate regression of each variable against the filtered time series of F_Q and its time derivative. The regression produces

[3] An additional peak is found near the annual period because of the variance found in superannual equatorial waves leaking into the subannual band. These waves do not appear to affect the stability of the MOC and so their discussion is relegated to the appendix.

two associated correlation patterns (ACPs; von Storch and Zwiers 1999) that are 90° out of phase and can capture propagating patterns. The full oscillation can be reconstructed by forming appropriate mixtures of the two ACPs.

a. *Multidecadal band*

The multidecadal oscillation is qualitatively similar to the Atlantic multidecadal oscillation (AMO; Kerr 2000; Hurrell et al. 2006) and consists of a basinwide fluctuation in the strength of the residual circulation wherein anomalies of ψ form in the NH Subpolar Gyre and propagate southward (Fig. 7). The fluctuations in ψ are associated with the advection of SST and sea surface salinity (SSS) anomalies in the NH Subpolar Gyre. The period of the oscillation is consistent with the time required for SSS perturbations to be advected around the subpolar gyre.

Two mechanisms for this type of multidecadal variability have been described in the literature. The first mechanism is large-scale baroclinic instability (Colin de Verdière and Huck 1999; te Raa and Dijkstra 2002; Dijkstra et al. 2014), whereby buoyancy anomalies generate zonal and meridional velocities in quadrature with each other, leading to a westward propagation that eventually reverses the sign of the buoyancy anomaly. The second growth mechanism only operates under mixed boundary conditions and relies on the positive correlation of SST and SSS fluctuations to generate buoyancy variance, despite the damping due to surface thermal relaxation (Weaver and Sarachick 1991a,b; Weaver et al. 1991, 1993; Arzel et al. 2006).

Arzel et al. (2006) showed that these two mechanisms can be distinguished by considering the budget of buoyancy variance, which—in the quasigeostrophic context—is proportional to the available potential energy (APE) of the eddy field (Lorenz 1955). The evolution of buoyancy is governed by

$$b_t + \mathbf{u}^\dagger \cdot \nabla b = \mathcal{D} + \mathcal{F}(b), \tag{16}$$

where $\mathbf{u}^\dagger \equiv \mathbf{u} + \mathbf{u}_{\rm GM}$ is the sum of the resolved and parameterized vector velocities, $\mathcal{D}$ represents the effect of diapycnal processes (e.g., diffusion and convection), and $\mathcal{F}(b)$ represents the surface flux of buoyancy. The surface flux term is nonzero only in the uppermost vertical grid cell. The buoyancy variance equation

$$\frac{\partial}{\partial t}\frac{1}{2}\overline{b'^2} + \nabla \cdot \frac{1}{2}\overline{\mathbf{u}^\dagger b'^2} = -\overline{\mathbf{u}'b'} \cdot \nabla \overline{b} + \overline{b'\mathcal{D}'} + \overline{b'\mathcal{F}(b')}, \tag{17}$$

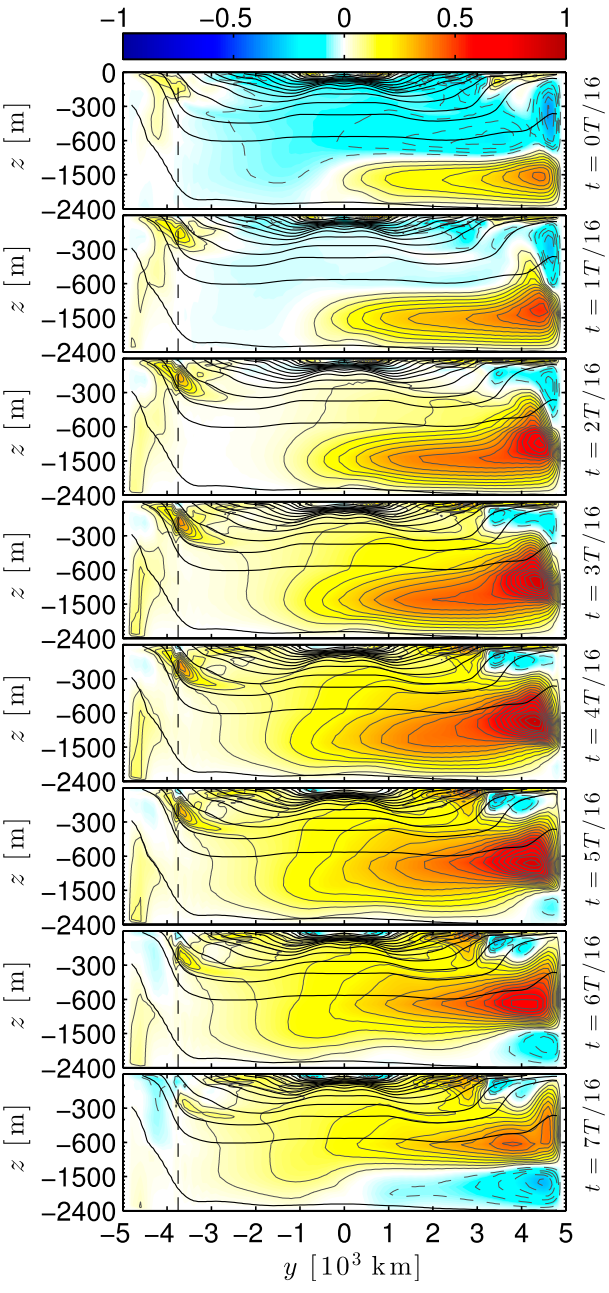

FIG. 7. Residual overturning streamfunction ψ anomalies in Sv through the first half period of the multidecadal oscillation reconstructed from the ACPs in the multidecadal band. The mean period is 21 ± 3 yr based on the location and half width of the decadal peak in the power spectrum. The panels are 1/16 of a period apart.

where $\mathbf{u}' \equiv \mathbf{u}^\dagger - \overline{\mathbf{u}^\dagger}$, is found by subtracting the time mean of (16) and multiplying the result by the perturbation buoyancy b'. Integrating over the volume of the fluid eliminates the divergence term on the lhs, resulting in

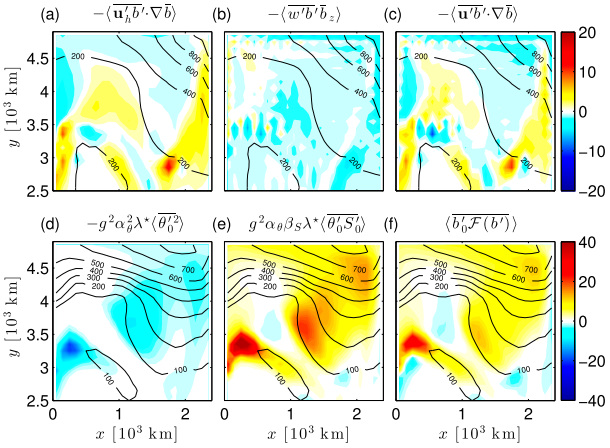

FIG. 8. Colors give the vertical integrals of production terms in the buoyancy variance equation in units of $10^{-12}\,\mathrm{m^3\,s^{-5}}$. The terms shown are (a) horizontal downgradient buoyancy flux, (b) vertical downgradient buoyancy flux, (c) total downgradient buoyancy flux, (d) variance destruction by surface thermal damping, (e) variance production by correlated surface thermohaline perturbations, and (f) total surface production of variance. Note that the color range of the lower panels is twice that of the upper panels. Contours give the mean and standard deviation of the mixed layer depth in the upper and lower panels, respectively.

$$\frac{d}{dt}\int \frac{1}{2}\overline{b'^2}\,\mathrm{d}V = -\int \overline{u'b'}\cdot\nabla\overline{b}\,\mathrm{d}V + \Delta z_1 \int \overline{b_0'\mathcal{F}(b')}\,dA + \int \overline{b'\mathcal{D}'}\,dV, \qquad (18)$$

where Δz_1 is the thickness of the uppermost vertical grid cell, and b_0 is the surface buoyancy. In a statistically steady state, the lhs vanishes and the three terms on the rhs must balance each other. The last term on the rhs is negative definite since the effect of diffusion is to destroy buoyancy variance; thus, the sum of the first two terms must be positive.

The first term on the rhs of (17) represents buoyancy variance generated by downgradient buoyancy fluxes (DGBF). For large-scale flows, this term is typically associated with baroclinic instability. Specifically, the horizontal component of the DGBF $-\overline{\mathbf{u}_h' b'}\cdot\nabla_h\overline{b}$ is proportional to the conversion of mean APE to eddy APE and the vertical component of the DGBF $-\overline{w'b'}\,\overline{b}_z$ is proportional to the conversion of eddy kinetic energy to eddy APE (e.g., Beckmann et al. 1994).

If the buoyancy boundary condition is either fixed flux or fixed value, $\overline{b_0'\mathcal{F}(b')} = 0$, and baroclinic instability is the only mechanism that can drive large-scale variability (assuming that Reynolds stresses are negligible on large scales). However, for the mixed boundary conditions used in the present experiments,

TABLE 2. Buoyancy variance production terms integrated over the region shown in Fig. 8 ($y > 2500$ km) and integrated over the entire domain. The units are $\mathrm{m^5\,s^{-5}}$.

Term	Net ($y > 2500$ km)	Net (global)
$-\overline{\mathbf{u}_h' b'}\cdot\nabla_h\overline{b}$	5.7	7.9
$-\overline{w'b'}\,\overline{b}_z$	−3.3	−5.2
$-\lambda^\star g^2\alpha_\theta^2\overline{\theta_0'^2}$	−11.6	−13.3
$\lambda^\star g^2\beta_S^2\overline{\theta_0' S_0'}$	31.7	35.0
$-\overline{\mathbf{u}' b'}\cdot\nabla\overline{b}$	2.4	2.8
$\overline{b'\mathcal{F}(b')}$	20.1	22.7
Total production	22.5	25.5

$$\overline{b_0'\mathcal{F}(b')} = g^2\alpha_\theta\lambda^\star(\beta_S\overline{\theta_0' S_0'} - \alpha_\theta\overline{\theta_0'^2}), \qquad (19)$$

where $\lambda^\star = (10\ \mathrm{days})^{-1}$ is the temperature relaxation rate. This surface production term is positive if SSS and SST are positively correlated and surface buoyancy perturbations are dominated by salinity perturbations (Arzel et al. 2006).

The vertical integrals of the production terms in (17) are shown in Fig. 8 (denoted by angle brackets) for the NH Subpolar Gyre, and the values of the production terms, integrated over the NH Subpolar Gyre and the entire domain, are given in Table 2. In both cases, the perturbation quantities are defined using the multidecadal bandpass filter defined in (14). The NH Subpolar Gyre accounts for more than 85% of the variance produced by DGBF and 88% of the surface buoyancy variance production.

The conversion of mean APE to eddy APE (Fig. 8a) is largely offset by conversion of eddy APE to eddy kinetic energy (Fig. 8b). The net DGBF is characterized by locally large positive and negative values that integrate to a small positive value (Fig. 8c; Table 2). Baroclinic instability thus gives a small but positive contribution to the buoyancy variance budget. However, the thermal field is highly damped by surface temperature relaxation; the rate of destructure of buoyancy variance by thermal relaxation exceeds production by baroclinic instability by almost a factor of 5 (Fig. 8d; Table 2). The observed multidecadal variability thus cannot be sustained by baroclinic instability alone. Additional buoyancy variance is produced by correlations between SST and SSS—in fact, this production term dominates the buoyancy variance budget so that net buoyancy variance production is positive.

Figure 8 also shows the mean mixed layer depth (upper panels) and standard deviation of the mixed layer depth (lower panels). A local maximum in surface buoyancy variance production in the northeast corner at $(x, y) = (2050, 4550)$ km is near where the

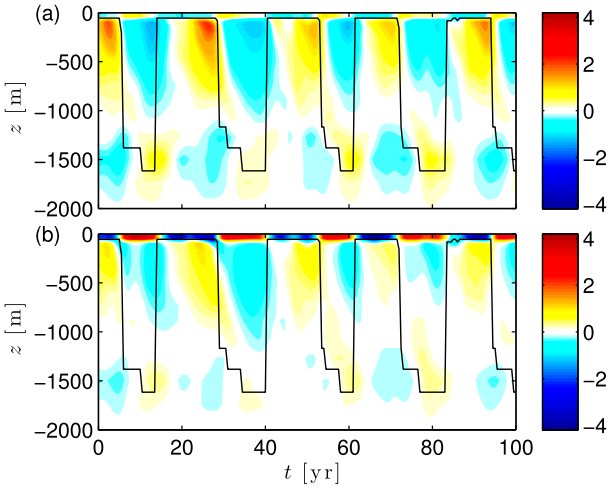

FIG. 9. Depth–time contours of (a) temperature ($g\alpha_\theta\theta'$) and (b) salinity ($g\beta_S S'$) perturbations in the decadal band, in buoyancy units, in the northeastern corner of the domain, where surface production has a local maximum. The (unfiltered) mixed layer depth is plotted in black.

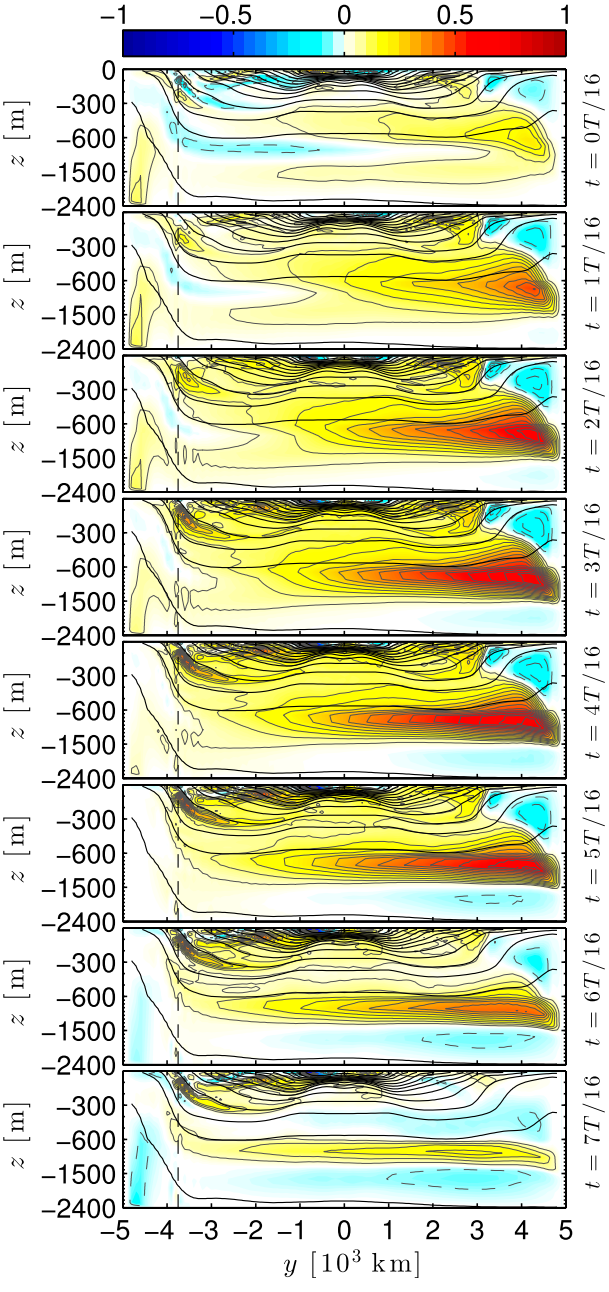

FIG. 10. Residual streamfunction anomalies in Sv through the first half-period of the multicentennial oscillation reconstructed from the ACPs in the multicentennial band. The mean period is 380 ± 60 yr. The panels are 1/16 of a period apart.

mixed layer is deepest on average and just upstream of a local maximum in the mixed layer depth variability.

The vertical/time structure of the thermohaline fluctuations is illustrated in Fig. 9. Temperature and salinity perturbations are positively correlated with each other throughout the water column. The signs of the perturbations reverse at the base of the mixed layer and again below 1250-m depth. This vertical structure is key to maintaining the oscillation, which proceeds as follows: The arrival of a salty anomaly (at, e.g., $t = 5$ yr) destabilizes the water column, triggering convection. As the mixed layer deepens, cold water is brought to the surface from below the mixed layer, further destabilizing the water column and feeding the growth of the oscillation. (The water below the mixed layer is also anomalously fresh but sufficiently cold that the thermal effect dominates.) The mixed layer eventually deepens sufficiently that convection taps warm water from below $z = -1250$ m, stabilizing the water column and shutting off convection. The cycle then repeats with opposite-signed perturbations and anomalous negative convection.

b. *Multicentennial band*

The multicentennial mode is characterized by a strengthening and weakening of the residual streamfunction ψ, which is nearly synchronous with latitude (Figs. 10, 11a). The overturning anomalies are associated with SSS anomalies that have both an antisymmetric component (i.e., with opposite signs between the hemispheres) and a symmetric component (Fig. 11b). The oscillation is also accompanied by a periodic widening and shrinking of the regions of surface isopycnals shared between the NH and the channel (Fig. 12).

SSS anomalies are dominated by the antisymmetric component; the leading EOF of the antisymmetric

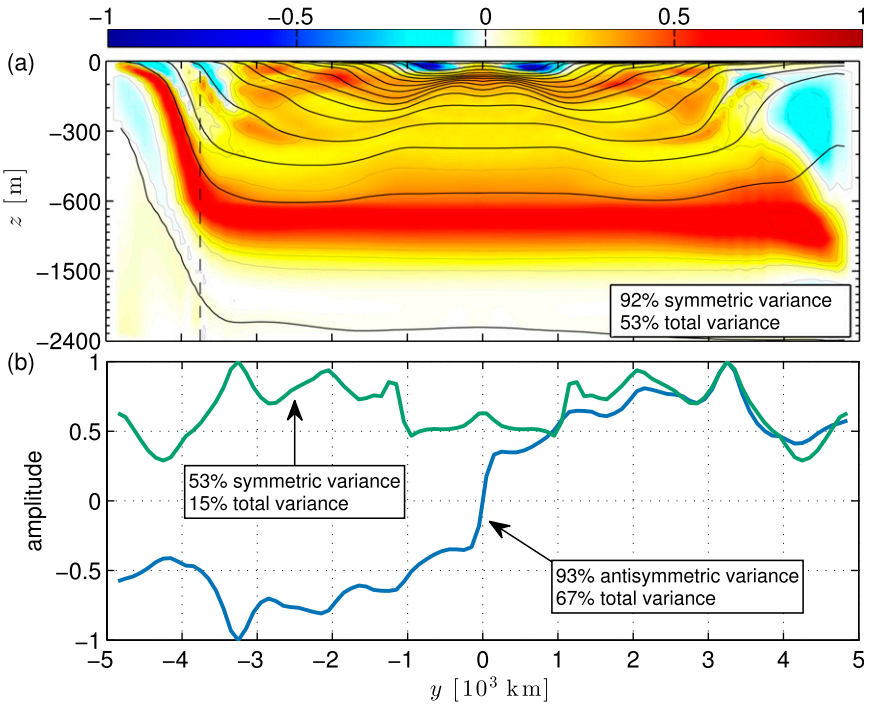

FIG. 11. Structure functions of the (a) first symmetric EOF of ψ and (b) the first antisymmetric (blue) and symmetric (green) EOFs of zonally averaged surface salinity. Insets give the variance explained by each of the EOFs. The EOFs are calculated in latitude/buoyancy space but plotted in height coordinates. This remapping results in a loss of the perfect symmetry that was present in the y–b plane.

part of the zonally averaged SSS captures 67% of the total variance (Fig. 11b). The principal component (PC) of the antisymmetric SSS is in phase with the PC of the leading EOF of the residual overturning. The second EOF of the symmetric component of the salinity anomaly is in approximate quadrature with the residual overturning; ψ lags the salt signal by about 86 yr.

Our model diagnostics indicate that ψ is dominated by an interhemispheric circulation that is symmetric around the equator both in the time-mean state (cf. Fig. 2a) and in the time-dependent fluctuations (cf. Fig. 11a). In contrast, the symmetric and antisymmetric components of the salinity field have comparable contributions both in the time-mean state (cf. Fig. 2c) and in the time-dependent anomalies (cf. Fig. 11b). The multicentennial oscillations found in our computations do not have the relaxation–oscillation character described in Sévellec et al. (2010).

The phase relations between the fluctuations of ψ and SSS suggest a simple model that considers the evolution of the zonally (but not time) averaged salinity in the surface mixed layer $S_m(y, t)$. In the mixed layer, salinity is assumed to be independent of z and the evolution of its zonal average is governed by

$$D\partial_t S_m + \psi_D(y,t)\partial_y S_m = -\mathcal{F} + \partial_y(Dk\partial_y S_m), \tag{20}$$

where ψ_D is the residual overturning at the base of the mixed layer, and k is the mixed layer diffusivity associated with the Redi coefficient. The mixed layer model assumes a balance between the advective flux of salt at the bottom of the mixed layer, given by $-\partial_y(\partial_z\psi_D S_m)$, and a horizontal salinity flux given by $\partial_z(\partial_y\psi S_m)$, accompanied by horizontal diffusive fluxes $-k\partial_y\bar{S}_m$. When integrated over the depth of the mixed layer D, the salinity budget becomes (20). Because of convective adjustment, D is larger than the imposed depth of the mixed layer d, defined in (1), and it is in general time and space dependent. However, in the following we will consider it a constant.

A predictive model relating ψ_D to S_m will not be explicitly considered here, as it is the subject of future studies. Instead, we use the mixed layer salinity budget [(20)], together with the diagnostics of our numerical results, to build a conceptual model of the multicentennial oscillation inspired by the Howard–Malkus–Welander

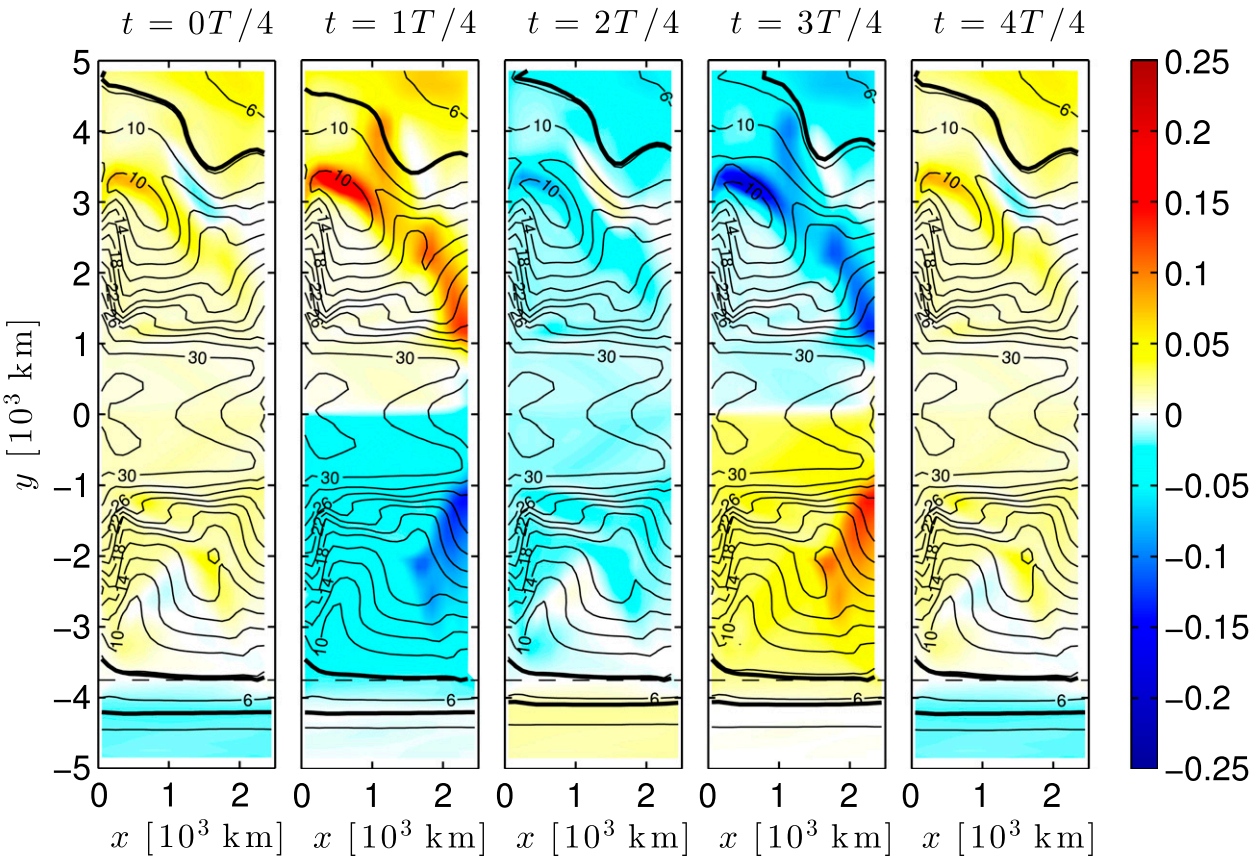

FIG. 12. SSS anomaly (colors) and total surface buoyancy (thin black contours) snapshots during the multicentennial oscillations. The thick black lines mark the boundaries of the surface isopycnals shared between the NH and the channel region. In the Northern Hemisphere, the southern edge of the shared isopycnals is marked by the position of the buoyancy at the northern edge of the channel $b = b_c$. In the Southern Hemisphere, the northern edge of the shared surface buoyancy is $b = b_c$, and the southern edge is the lowest buoyancy on the northern boundary of the domain $b = b_N$. The panels are 1/4 of a period apart.

loop model (Malkus 1972; Welander 1986). We thus proceed to examine the predictions of (20), assuming that we can project the symmetric and asymmetric EOFs of S_m and ψ_D onto simple sines and cosines; that is,

$$S_m = [\Gamma + s_s(t)]\cos(\pi y/L) + [\Delta + s_a(t)]\sin(\pi y/L),$$
$$\psi_D = \Psi + \psi'(t). \tag{21}$$

For ψ_D, we chose the simplest form of symmetric functions: a constant in space. The terms Ψ and ψ' denote the steady-state and time-dependent components of ψ_D, respectively; Γ and Δ denote the steady-state components of the symmetric and antisymmetric parts of S_m, respectively, while s_s and s_a are the time-dependent fluctuations. Substituting (21) into (20) and projecting onto the spatial modes, we obtain

$$\dot{s}_s + \frac{\pi}{DL}(\Psi + \psi')(\Delta + s_a) = -\frac{\pi}{DL}\int_{-L}^{L} \mathcal{F}(y)\cos(\pi y/L)\,dy - \frac{\pi^2 k}{L^2}(\Gamma + s_s),$$
$$\dot{s}_a - \frac{\pi}{DL}(\Psi + \psi')(\Gamma + s_s) = -\frac{\pi}{DL}\int_{-L}^{L} \mathcal{F}(y)\sin(\pi y/L)\,dy - \frac{\pi^2 k}{L^2}(\Delta + s_a). \tag{22}$$

The positive correlation between the principal components of ψ' and of the antisymmetric salinity indicates that $\psi' = \lambda s_a$, with $\lambda > 0$. This relation is consistent with our finding that ψ increases as the buoyancy difference

between the channel and the northern boundary $b_C - b_N$ increases (cf. Figs. 4 and 5). Assuming that $\psi' \ll \Psi$ and $(s_a, s_s) \ll (\Gamma, \Delta)$, the evolution equations for the fluctuations are[4]

$$\dot{s}_s + \frac{\pi}{DL}(\Psi + \lambda\Delta)s_a = -\frac{\pi^2 k}{L^2}s_s, \tag{23}$$

$$\dot{s}_a - \frac{\pi}{DL}(\Psi s_s + \lambda\Gamma s_a) = -\frac{\pi^2 k}{L^2}s_a. \tag{24}$$

The system (24) is consistent with our finding that ψ' (or, equivalently, s_a) lags the symmetric salinity anomaly s_s by about one-quarter of an oscillation period. Thus, (24) describes an oscillator with frequency ω_r and growth rate ω_i given by

$$\omega_r = \frac{\pi}{L}\sqrt{\frac{\Psi}{D^2}(\Psi + \lambda\Delta) - \frac{\pi^2\lambda^2\Gamma^2}{4D^2} + \frac{\pi k}{DL}\lambda\Gamma},$$

$$\omega_i = \frac{\pi\lambda\Gamma}{2DL} - \frac{\pi^2 k}{L^2}. \tag{25}$$

The important point is that if λ and Γ are both positive—as is the case in our computations—and large enough to overcome the damping due to diffusion, then growth is possible. The arrangement of $(\lambda, \Gamma) > 0$ is the opposite of the original Howard–Malkus–Welander loop where both these quantities are negative, but both cases lead to growth. In the interhemispherical generalization of the Howard–Malkus–Welander loop considered by Sévellec et al. (2006), the parameter Γ in (25), which measures the symmetric component of the time- and zonally averaged SSS, is set to zero and thus growth is not possible. In our case, Fig. 2c shows that the zonally averaged SSS has both a symmetric and antisymmetric component (i.e., $\Gamma \neq 0$) and growing oscillations around this mean state are possible. Figure 2c should be contrasted with Fig. 3c where the SSS in the diffusive (reverse) cell is dominated by the antisymmetric component. In the adiabatic regime, the time-mean MOC is related to the symmetric component of the buoyancy (i.e., the shared buoyancy values), while in the Howard–Malkus–Welander loop the interhemispheric circulation depends only on the antisymmetric buoyancy component (i.e., it is down the buoyancy gradient).

Although the forward circulation never shuts down in the range of parameters of Figs. 10 and 12, near the critical point of transition between the forward- and reverse-cell regimes, the multicentennial oscillations increase in amplitude enough to shut off the forward (or reverse) cell. In this sense, the multicentennial oscillation mediates the transition between the regimes (cf. Fig. 4) of forward and reverse circulations.

5. Summary and conclusions

Oscillations on decadal and centennial time scales around multiple regimes are found in a model of the quasi-adiabatic overturning circulation. The essential elements for a quasi-adiabatic cell are isopycnals that surface in the high latitudes of both hemispheres, connecting a region where the flow is "pulled" by the Ekman suction in one hemisphere more than the other. The strongest pulling is affected in the reentrant region of the SH, leading to a forward cell with interior adiabatic flow along the shared isopycnals and diabatic flow in the surface mixed layer. This mechanically driven adiabatic cell is a globally attracting point in phase space around which trajectories cluster. However, it is also possible to have a reverse cell with shallow pulling in the subpolar region of the NH for the same set of parameters. This cell avoids the reentrant region in the SH and is wholly confined to the semienclosed portion of the domain. This reverse cell appears to be diffusively balanced, with amplitude vanishing in the limit where the interior diffusivity goes to zero.

The coexistence of both cells for some values of the forcing is due to the salt–advection feedback. With a symmetric freshwater forcing pattern of freshening in high latitudes and evaporation in the subtropics, the forward interhemispheric cell brings salt to the high latitudes of the NH. When the NH is warmer than the SH, this transport widens the range of surface isopycnals that are shared between the hemispheres, increasing the circulation. If the interhemispheric asymmetry of the prescribed freshwater flux makes the SH denser than the NH, the salt–advection feedback can also reinforce a cell in the opposite direction. The salt–advection feedback does not increase the density differences between hemispheres, unlike in the diffusive regime (Stommel 1961; Rooth 1982). In both the diffusive and quasi-adiabatic regimes, the salt–advection feedback is positive—it reinforces the circulation.

For an intermediate range of the freshwater flux asymmetry parameter, multiple regimes are found. For the low diffusivity used here, there are no steady states but rather regimes in which quasi-periodic solutions oscillate around a point in phase space. Because the amplitude of the oscillations increases with decreasing diffusivity, it is not possible to determine the full range of parameters where hysteresis exists using a model that

[4] The steady-state salinities Γ and Δ are determined by the leading order balance of (23), given the dependence of Ψ on the salinity and other parameters, a process whose study is deferred to future work.

time steps the equations of motion. We conjecture that the range of multiple states is wider than what we found but that the states are unstable to oscillatory perturbations.

We find that the oscillations peak at three time scales: superannual, multidecadal, and multicentennial scales. The three time scales also have distinct spatial structures. The superannual component is an equatorially trapped wave generated by baroclinic instability of the tropical gyres. The multidecadal component of the oscillation is characterized by perturbations that are confined to the NH Subpolar Gyre that arise from a surface thermohaline instability.

The multicentennial oscillation is expressed in both hemispheres with large-scale patterns of SSS that have opposite signs in the semienclosed portions of the opposing hemispheres. The multicentennial oscillation arises because a symmetric component of SSS anomalies is generated by advection of antisymmetric anomalies. The symmetric SSS anomalies are in quadrature with the antisymmetric component. Antisymmetric SSS anomalies are amplified by advection of the large-scale equator-to-pole salinity gradient by time-dependent increase/decrease of the interhemispheric cell. Because the latter is positively correlated with the antisymmetric component of the SSS, growth is possible for weak enough diffusion. The alternating increase and decrease of the overturning strength leads to oscillations that, for large enough amplitude, switch to the regime of reverse overturning. Indeed, the amplification of the multidecadal and multicentennial oscillations is an indication of the impending transition to a different regime and potentially an index for anticipating abrupt change.

Acknowledgments. CLW and PC are supported by the Office of Science (BER), U.S. Department of Energy under Grant DE-SC0005100, and the National Science Foundation under Grant OCE-1258887. Computational resources were provided by the National Energy Research Scientific Computing Center.

APPENDIX

Superannual Oscillation

Figure A1a shows a small segment of a time series of F_Q in a LOW-DIFF experiment with $\Delta F = -0.03$ Sv and the MOC in the "forward" state (cf. Fig. 4). Oscillations with a period of approximately a year are evident, modulated on interannual and multidecadal time scales. The high-frequency signal (Fig. A1b) is the difference between the unfiltered time series and the time series low-passed using the filter in (14) with $\tau_{\text{low}} = 5$ yr and $\tau_{\text{high}} = \infty$. We will refer to the high-frequency signal as the "annual-band" signal, even though it contains range of periods centered on the annual period.

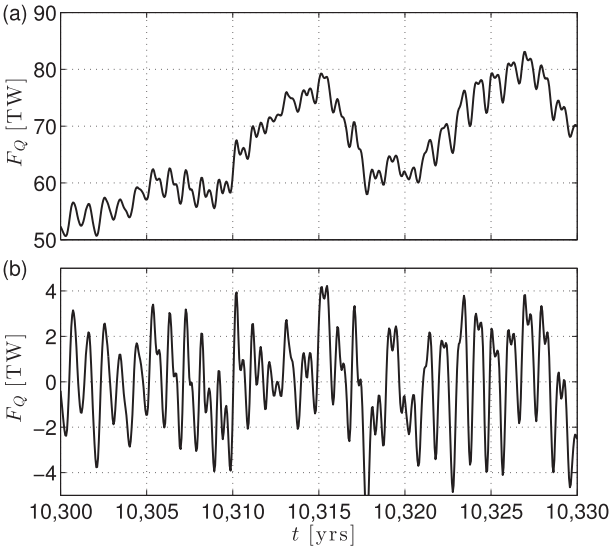

FIG. A1. (a) Time series of cross-equatorial heat flux F_Q for the same experiment shown in Fig. 6 but at a temporal resolution of 18.25 days to show the annual cycle. (b) The annual-band component of the time series shown in (a).

The forcing is steady and no seasonal modulation is imposed, so the emergence of an annual time scale is purely coincidental and not associated with the seasonal cycle. Indeed, the period of the oscillation is 354 days—slightly shorter than a year—with a harmonic at 179 days. The associated meridional velocity field is shown in Figs. A2 and A3. The spatial structure resembles a second baroclinic mode equatorial Rossby wave with zonal and meridional wavenumbers 3 and 1, respectively, "leaning" into the horizontal and vertical shear. The disturbance propagates westward at an average speed of about 0.03 m s^{-1}.

An equatorial Rossby wave with zonal and meridional wavenumbers k and n propagating through an unsheared, resting fluid has phase speed

$$c_R = -\frac{\beta}{k^2 + (2n+1)\beta/c}, \tag{A1}$$

where c is the phase speed associated with the vertical mode number (Gill 1982). In the present case, $c \approx 0.8$ m s^{-1}, so $c_R \approx 0.16$ m s^{-1}, which is significantly faster than the speed the disturbance shows in Figs. A2 and A3. The observed wave is also broader than

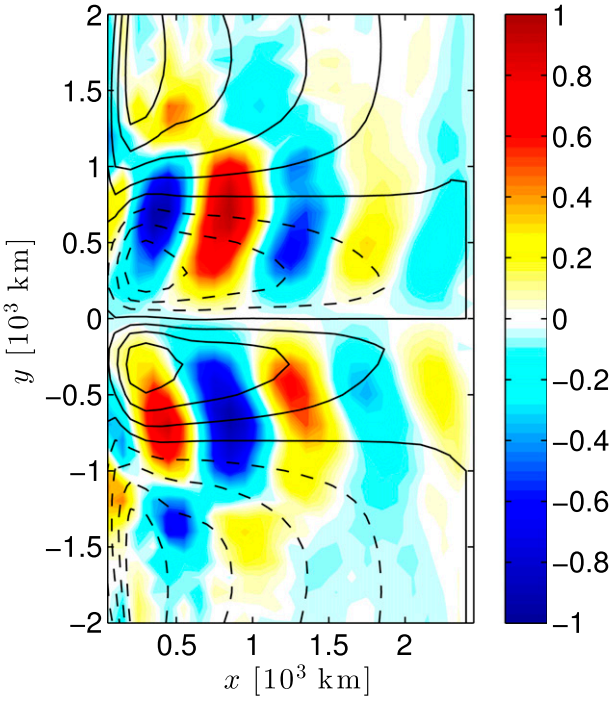

FIG. A2. Plan view of the leading EOF of annual-band meridional velocity shown at 100-m depth (colors with arbitrary scale) and barotropic streamfunction (contours with interval 2 Sv; negative contours are dashed). The second EOF is identical to the first but shifted a quarter wavelength in space. The leading pair explain 94% of the global variance of meridional velocity in the annual band.

an unsheared Rossby wave, with the maximum velocity found at $|y| \approx 650$ km rather than at $|y| = L_R$, where

$$L_R = \sqrt{\frac{c}{\beta}} \tag{A2}$$

in the equatorial Rossby radius; here, $L_R \approx 191$ km. These discrepancies can be explained by noting that the disturbance is propagating in a horizontally and vertically sheared background flow, which has been shown to slow and broaden equatorial Rossby waves (Philander 1979).

The origin of this mode is an instability of the tight tropical gyre driven by the wind stress imposed near the equator (cf. Fig. A2). Analysis of the time-mean Ertel potential vorticity

$$q = \overline{(f+\zeta)b_z} - \overline{v_z b_x} + \overline{u_z b_y} \tag{A3}$$

shows a reversal in the meridional gradient of q, with negative q_y in the region of westward flow of the tropical gyres (Fig. A4). Maxima of the baroclinic conversion rate $\overline{wb}$ are found just below and equatorward of the sign reversal of q_y and are collocated with the maximum amplitude of the

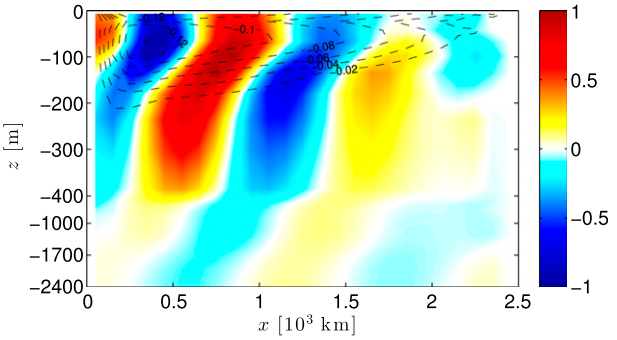

FIG. A3. Zonal section of the leading EOF of annual-band meridional velocity shown at $y = 600$ km (colors with arbitrary scale) and mean zonal velocity (contours with interval 2 cm s^{-1}); negative contours are dashed and the zero contour is omitted. Note the change in vertical scale below 400 m.

disturbance (Fig. A4b), indicating that the origin of this mode is likely baroclinic instability of the vertically sheared tropical gyres (the horizontal shear production terms are negligible). The equatorial deformation radius L_R is marginally resolved in this coarse-resolution model, allowing the instability, and its associated time dependence, to develop. Similar modes have been described by Cox (1985), who found periods of 100 and 50 days. These periods are shorter than in our case, likely because the southern

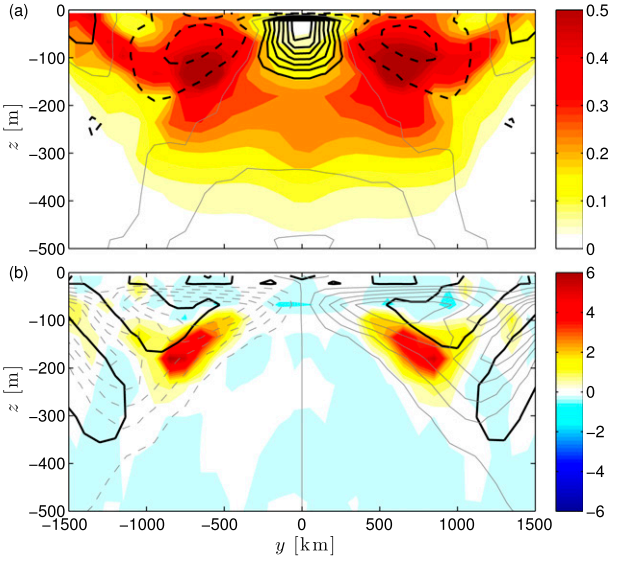

FIG. A4. (a) Kinetic energy of the high-passed flow in 10^{-3} J kg^{-1} (colors) and mean zonal velocity (contours). The contour interval is 10 cm s^{-1}; negative contours are dashed, and the zero contour is gray. (b) Baroclinic conversion rate $\overline{wb}$ of the high-passed flow in 10^{-9} W kg^{-1} (colors) and mean Ertel potential vorticity q (gray contours). The contour interval is 5×10^{-10} s^{-3}; negative contours are dashed. The thick black contours show where the meridional gradient of the EPV changes sign. Both panels are meridional sections at $x = 650$ km.

boundary of Cox's model was located at the equator, precluding the development of strong shear in the tropical gyres.

REFERENCES

Arzel, O., T. Huck, and A. Colin de Verdière, 2006: The different nature of the interdecadal variability of the thermohaline circulation under mixed and flux boundary conditions. *J. Phys. Oceanogr.,* **36,** 1703–1718, doi:10.1175/JPO2938.1.

Beckmann, A., C. W. Böning, B. Brügge, and D. Stammer, 1994: On the generation and role of eddy variability in the central North Atlantic Ocean. *J. Geophys. Res.,* **99,** 20 381–20 391, doi:10.1029/94JC01654.

Bryan, F., 1986: High-latitude salinity effects and interhemispheric thermohaline circulations. *Nature,* **323,** 301–304, doi:10.1038/323301a0.

Buckley, M. W., D. Ferreira, J.-M. Campin, J. Marshall, and R. Tulloch, 2012: On the relationship between decadal buoyancy anomalies and variability of the Atlantic meridional overturning circulation. *J. Climate,* **25,** 8009–8030, doi:10.1175/JCLI-D-11-00505.1.

Cessi, P., and W. R. Young, 1992: Multiple equilibria in two-dimensional thermohaline circulation. *J. Fluid Mech.,* **241,** 291–309, doi:10.1017/S0022112092002040.

Cimatoribus, A. A., S. S. Drijfhout, and H. A. Dijkstra, 2014: Meridional overturning circulation: Stability and ocean feedbacks in a box model. *Climate Dyn.,* **42,** 311–328, doi:10.1007/s00382-012-1576-9.

Colin de Verdière, A., and T. Huck, 1999: Baroclinic instability: An oceanic wavemaker for interdecadal variability. *J. Phys. Oceanogr.,* **29,** 893–910, doi:10.1175/1520-0485(1999)029<0893:BIAOWF>2.0.CO;2.

Cox, M. D., 1985: An eddy resolving numerical model of the ventilated thermocline. *J. Phys. Oceanogr.,* **15,** 1312–1324, doi:10.1175/1520-0485(1985)015<1312:AERNMO>2.0.CO;2.

Danabasoglu, G., and J. C. McWilliams, 1995: Sensitivity of the global ocean circulation to parameterizations of mesoscale tracer transports. *J. Climate,* **8,** 2967–2987, doi:10.1175/1520-0442(1995)008<2967:SOTGOC>2.0.CO;2.

de Szoeke, R. A., and A. F. Bennett, 1993: Microstructure fluxes across density surfaces. *J. Phys. Oceanogr.,* **23,** 2254–2264, doi:10.1175/1520-0485(1993)023<2254:MFADS>2.0.CO;2.

Dijkstra, H. A., 2007: Characterization of the multiple equilibria regime in a global ocean model. *Tellus,* **59A,** 695–705, doi:10.1111/j.1600-0870.2007.00267.x.

——, and M. Ghil, 2005: Low-frequency variability of the large-scale ocean circulation: A dynamical systems approach. *Rev. Geophys.,* **43,** RG3002, doi:10.1029/2002RG000122.

——, J. A. Saenz, and A. M. Hogg, 2014: Energetics of multidecadal Atlantic Ocean variability. *J. Climate,* **27,** 7874–7889, doi:10.1175/JCLI-D-12-00801.1.

Ferrari, R., S. M. Griffies, A. J. G. Nurser, and G. K. Vallis, 2010: A boundary-value problem for the parameterized mesoscale eddy transport. *Ocean Modell.,* **32,** 143–156, doi:10.1016/j.ocemod.2010.01.004.

Fürst, J. J., and A. Levermann, 2012: A minimal model for wind- and mixing-driven overturning: Threshold behavior for both driving mechanisms. *Climate Dyn.,* **38,** 239–260, doi:10.1007/s00382-011-1003-7.

Ganachaud, A., and C. Wunsch, 2003: Large-scale ocean heat and freshwater transports during the World Ocean Circulation Experiment. *J. Climate,* **16,** 696–705, doi:10.1175/1520-0442(2003)016<0696:LSOHAF>2.0.CO;2.

Gent, P. R., and J. C. McWilliams, 1990: Isopycnal mixing in ocean circulation models. *J. Phys. Oceanogr.,* **20,** 150–155, doi:10.1175/1520-0485(1990)020<0150:IMIOCM>2.0.CO;2.

Gill, A. E., 1982: *Atmosphere–Ocean Dynamics.* Academic Press, 682 pp.

Gnanadesikan, A., 1999: A simple predictive model for the structure of the oceanic pycnocline. *Science,* **283,** 2077–2079, doi:10.1126/science.283.5410.2077.

——, and J. R. Toggweiler, 1999: Constraints placed by silicon cycling on vertical exchange in general circulation models. *Geophys. Res. Lett.,* **26,** 1865–1868, doi:10.1029/1999GL900379.

Greatbatch, R. J., and S. Zhang, 1995: An interdecadal oscillation in an idealized ocean basin forced by constant heat flux. *J. Climate,* **8,** 81–91, doi:10.1175/1520-0442(1995)008<0081:AIOIAI>2.0.CO;2.

Gregg, M. C., T. B. Sanford, and D. P. Winkel, 2003: Reduced mixing from the breaking of internal waves in equatorial waters. *Nature,* **422,** 513–515, doi:10.1038/nature01507.

Griffies, S. M., R. C. Pacanowski, and R. W. Hallberg, 2000: Spurious diapycnal mixing associated with advection in a *z*-coordinate ocean model. *Mon. Wea. Rev.,* **128,** 538–564, doi:10.1175/1520-0493(2000)128<0538:SDMAWA>2.0.CO;2.

Grossmann, I., and P. J. Klotzbach, 2009: A review of North Atlantic modes of natural variability and their driving mechanisms. *J. Geophys. Res.,* **114,** D24107, doi:10.1029/2009JD012728.

Haney, R. L., 1971: Surface thermal boundary condition for ocean circulation models. *J. Phys. Oceanogr.,* **1,** 241–248, doi:10.1175/1520-0485(1971)001<0241:STBCFO>2.0.CO;2.

Hofmann, M., and M. A. Morales Maqueda, 2006: Performance of a second-order moments advection scheme in an ocean general circulation model. *J. Geophys. Res.,* **111,** C05006, doi:10.1029/2005JC003279.

——, and S. Rahmstorf, 2009: On the stability of the Atlantic meridional overturning circulation. *Proc. Natl. Acad. Sci. USA,* **106,** 20 584–20 589, doi:10.1073/pnas.0909146106.

Huang, R. X., and R. L. Chou, 1994: Parameter sensitivity study of the saline circulation. *Climate Dyn.,* **9,** 391–409, doi:10.1007/BF00207934.

Huck, T., A. Colin de Verdière, and A. J. Weaver, 1999: Interdecadal variability of the thermohaline circulation in box-ocean models forced by fixed surface fluxes. *J. Phys. Oceanogr.,* **29,** 865–892, doi:10.1175/1520-0485(1999)029<0865:IVOTTC>2.0.CO;2.

——, O. Arzel, and F. Sévellec, 2015: Multidecadal variability of the overturning circulation in presence of eddy turbulence. *J. Phys. Oceanogr.,* **45,** 157–173, doi:10.1175/JPO-D-14-0114.1.

Hurrell, J. W., and Coauthors, 2006: Atlantic climate variability and predictability: A CLIVAR perspective. *J. Climate,* **19,** 5100–5121, doi:10.1175/JCLI3902.1.

Johnson, H. L., D. P. Marshall, and D. A. J. Sproson, 2007: Reconciling theories of a mechanically driven meridional overturning circulation with thermohaline forcing and multiple equilibria. *Climate Dyn.,* **29,** 821–836, doi:10.1007/s00382-007-0262-9.

Kara, A. B., P. A. Rochford, and H. E. Hurlburt, 2000: An optimal definition for the ocean mixed layer. *J. Geophys. Res.,* **105,** 16 803–16 821, doi:10.1029/2000JC900072.

Keeling, R. F., 2002: On the freshwater forcing of the thermohaline circulation in the limit of low diapycnal diffusivity. *J. Geophys. Res.,* **107,** C73077, doi:10.1029/2000JC000685.

Kerr, R. A., 2000: A North Atlantic pacemaker for the centuries. *Science,* **288,** 1984–1986, doi:10.1126/science.288.5473.1984.

Kunze, E., and T. Sanford, 1996: Abyssal mixing: Where it is not. *J. Phys. Oceanogr.,* **26,** 2286–2286, doi:10.1175/1520-0485(1996)026<2286:AMWIIN>2.0.CO;2.

——, E. Firing, J. M. Hummon, T. K. Chereskin, and A. M. Thurnherr, 2006: Global abyssal mixing inferred from lowered ADCP shear and CTD strain profiles. *J. Phys. Oceanogr.,* **36,** 1553–1576, doi:10.1175/JPO2926.1.

Ledwell, J. R., A. J. Watson, and C. S. Law, 1993: Evidence for slow mixing across the pycnocline from an open-ocean tracer-release experiment. *Nature,* **364,** 701–703, doi:10.1038/364701a0.

Liu, Z., 2012: Dynamics of interdecadal climate variability: A historical perspective. *J. Climate,* **25,** 1963–1995, doi:10.1175/2011JCLI3980.1.

——, and Coauthors, 2009: Transient simulation of last deglaciation with a new mechanism for Bølling-Allerød warming. *Science,* **325,** 310–314, doi:10.1126/science.1171041.

Lorenz, E. N., 1955: Available potential energy and the maintenance of the general circulation. *Tellus,* **7,** 157–167, doi:10.1111/j.2153-3490.1955.tb01148.x.

Malkus, W. V. R., 1972: Non-periodic convection at high and low Prandtl number. *Mem. Soc. Roy. Sci. Liége,* **4,** 125–128.

Marshall, J., and K. Speer, 2012: Closure of the meridional overturning circulation through Southern Ocean upwelling. *Nat. Geosci.,* **5,** 171–180, doi:10.1038/ngeo1391.

——, A. Adcroft, C. Hill, L. Perelman, and C. Heisey, 1997a: A finite-volume, incompressible Navier Stokes model for studies of the ocean on parallel computers. *J. Geophys. Res.,* **102,** 5753–5766, doi:10.1029/96JC02775.

——, C. Hill, L. Perelman, and A. Adcroft, 1997b: Hydrostatic, quasi-hydrostatic, and nonhydrostatic ocean modeling. *J. Geophys. Res.,* **102,** 5733–5752, doi:10.1029/96JC02776.

McDougall, T. J., and P. C. McIntosh, 2001: The temporal-residual-mean velocity. Part II: Isopycnal interpretation and the tracer and momentum equations. *J. Phys. Oceanogr.,* **31,** 1222–1246, doi:10.1175/1520-0485(2001)031<1222:TTRMVP>2.0.CO;2.

McManus, J. F., R. Francois, J.-M. Gherardi, L. D. Keigwin, and S. Brown-Leger, 2004: Collapse and rapid resumption of Atlantic meridional circulation linked to deglacial climate changes. *Nature,* **428,** 834–837, doi:10.1038/nature02494.

Munk, W. H., 1966: Abyssal recipes. *Deep-Sea Res. Oceanogr. Abstr.,* **13,** 707–730, doi:10.1016/0011-7471(66)90602-4.

Nikurashin, M., and G. Vallis, 2012: A theory of the interhemispheric meridional overturning circulation and associated stratification. *J. Phys. Oceanogr.,* **42,** 1652–1667, doi:10.1175/JPO-D-11-0189.1.

Nof, D., S. Van Gorder, and A. de Boer, 2007: Does the Atlantic meridional overturning cell really have more than one stable steady state? *Deep-Sea Res. I,* **54,** 2005–2021, doi:10.1016/j.dsr.2007.08.006.

Philander, S. G. H., 1979: Equatorial waves in the presence of the Equatorial Undercurrent. *J. Phys. Oceanogr.,* **9,** 254–262, doi:10.1175/1520-0485(1979)009<0254:EWITPO>2.0.CO;2.

Prange, M., G. Lohmann, and A. Paul, 2003: Influence of vertical mixing on the thermohaline hysteresis: Analysis of an OGCM. *J. Phys. Oceanogr.,* **33,** 1707–1721, doi:10.1175/2389.1.

Prather, M. J., 1986: Numerical advection by conservation of second-order moments. *J. Geophys. Res.,* **91,** 6671–6681, doi:10.1029/JD091iD06p06671.

Rahmstorf, S., 1996: On the freshwater forcing and transport of the Atlantic thermohaline circulation. *Climate Dyn.,* **12,** 799–811, doi:10.1007/s003820050144.

——, 2000: The thermohaline ocean circulation: A system with dangerous thresholds? *Climatic Change,* **46,** 247–256, doi:10.1023/A:1005648404783.

——, and Coauthors, 2005: Thermohaline circulation hysteresis: A model intercomparison. *Geophys. Res. Lett.,* **32,** L23605, doi:10.1029/2005GL023655.

Redi, M. H., 1982: Oceanic isopycnal mixing by coordinate rotation. *J. Phys. Oceanogr.,* **12,** 1154–1158, doi:10.1175/1520-0485(1982)012<1154:OIMBCR>2.0.CO;2.

Rooth, C., 1982: Hydrology and ocean circulation. *Prog. Oceanogr.,* **11,** 131–149, doi:10.1016/0079-6611(82)90006-4.

Samelson, R. M., 2004: Simple mechanistic models of middepth meridional overturning. *J. Phys. Oceanogr.,* **34,** 2096–2103, doi:10.1175/1520-0485(2004)034<2096:SMMOMM>2.0.CO;2.

Schlesinger, M. E., J. Yin, G. Yohe, N. G. Andronova, S. Malyshev, and B. Li, 2006: Assessing the risk of a collapse of the Atlantic thermohaline circulation. *Proc. Avoiding Dangerous Climate Change: A Scientific Symp. on Stabilisation of Greenhouse Gases,* Exeter, United Kingdom, Met Office, 37–47.

Schmitner, A., M. Latif, and B. Schneider, 2005: Model projections of the North Atlantic thermohaline circulation for the 21st century assessed by observations. *Geophys. Res. Lett.,* **32,** L23710, doi:10.1029/2005GL024368.

Sévellec, F., T. Huck, and M. Ben Jelloul, 2006: On the mechanism of centennial thermohaline oscillations. *J. Mar. Res.,* **64,** 355–392, doi:10.1357/002224006778189608.

——, ——, and A. Colin de Verdière, 2010: From centennial to millennial oscillation of the thermohaline circulation. *J. Mar. Res.,* **68,** 723–742, doi:10.1357/002224011795977635.

Stommel, H., 1961: Thermohaline convection with two stable regimes of flow. *Tellus,* **13,** 224–230, doi:10.1111/j.2153-3490.1961.tb00079.x.

Talley, L. D., 2013: Closure of the global overturning circulation through the Indian, Pacific, and Southern Oceans: Schematics and transports. *Oceanography,* **26** (1), 80–97, doi:10.5670/oceanog.2013.07.

te Raa, L. A., and H. A. Dijkstra, 2002: Instability of the thermohaline ocean circulation on interdecadal timescales. *J. Phys. Oceanogr.,* **32,** 138–160, doi:10.1175/1520-0485(2002)032<0138:IOTTOC>2.0.CO;2.

Toggweiler, J. R., and B. Samuels, 1995: Effect of Drake Passage on the global thermohaline circulation. *Deep-Sea Res. I,* **42,** 477–500, doi:10.1016/0967-0637(95)00012-U.

von Storch, H., and F. W. Zwiers, 1999: *Statistical Analysis in Climate Research.* Cambridge University Press, 484 pp.

Waterman, S., K. L. Polzin, A. C. Naveira Garabato, K. L. Sheen, and A. Forryan, 2014: Suppression of internal wave breaking in the Antarctic Circumpolar Current near topography. *J. Phys. Oceanogr.,* **44,** 1466–1492, doi:10.1175/JPO-D-12-0154.1.

Weaver, A. J., and E. S. Sarachick, 1991a: Evidence for decadal variability in an ocean general circulation model: An advective mechanism. *Atmos.–Ocean,* **29,** 197–231, doi:10.1080/07055900.1991.9649403.

——, and ——, 1991b: The role of mixed boundary conditions in numerical models of the ocean's climate. *J. Phys. Oceanogr.,* **21,** 1470–1493, doi:10.1175/1520-0485(1991)021<1470:TROMBC>2.0.CO;2.

——, ——, and J. Marotzke, 1991: Freshwater flux forcing of decadal and interdecadal oceanic variability. *Nature,* **353,** 836–838, doi:10.1038/353836a0.

——, J. Marotzke, P. F. Cummins, and E. S. Sarachick, 1993: Stability and variability of the thermohaline circulation. *J. Phys. Oceanogr.,* **23,** 39–60, doi:10.1175/1520-0485(1993)023<0039:SAVOTT>2.0.CO;2.

Welander, P., 1986: Thermohaline effects in the ocean circulation and related simple models. *Large-Scale Transport Processes in Oceans and Atmosphere,* J. Willebrand and D. L. T. Anderson, Eds., NATO Science Series C, Vol. 190, Springer, 163–200.

Wolfe, C. L., and P. Cessi, 2010: What sets the strength of the middepth stratification and overturning circulation in eddying ocean models? *J. Phys. Oceanogr.,* **40,** 1520–1538, doi:10.1175/2010JPO4393.1.

——, and ——, 2011: The adiabatic pole-to-pole overturning circulation. *J. Phys. Oceanogr.,* **41,** 1795–1810, doi:10.1175/2011JPO4570.1.

——, and ——, 2014: Salt feedback in the adiabatic overturning circulation. *J. Phys. Oceanogr.,* **44,** 1175–1194, doi:10.1175/JPO-D-13-0154.1.

Young, W. R., 2012: An exact thickness-weighted average formulation of the Boussinesq equations. *J. Phys. Oceanogr.,* **42,** 692–707, doi:10.1175/JPO-D-11-0102.1.

Zhang, S., R. J. Greatbatch, and C. A. Lin, 1993: A reexamination of the polar halocline catastrophe and implications for coupled ocean–atmosphere modeling. *J. Phys. Oceanogr.,* **23,** 287–299, doi:10.1175/1520-0485(1993)023<0287:AROTPH>2.0.CO;2.